MARCH 07 2024

Comprehensive analysis of the seismic wave fields generated by offshore pile driving: A case study at the BARD Offshore 1 offshore wind farm

Tobias Bohne; Tanja Grießmann; Raimund Rolfes

J. Acoust. Soc. Am. 155, 1856–1867 (2024)
https://doi.org/10.1121/10.0025177

JASA ARTICLE

Comprehensive analysis of the seismic wave fields generated by offshore pile driving: A case study at the BARD Offshore 1 offshore wind farm

Tobias Bohne,[a] Tanja Grießmann, and Raimund Rolfes
Leibniz University Hannover, Institute of Structural Analysis, Appelstrasse 9a, 30167 Hannover, Germany

ABSTRACT:
Offshore pile driving not only generates high sound pressure levels, but also induces ground vibrations and particle motions that have the potential to affect fish and invertebrates living near or in the seabed. In particular, the seismic wave field in the form of interface waves is thought to be responsible for causing these particle motions and ground vibrations. However, the magnitude and spatial extent of the seismic wave field resulting from pile driving has not been clearly established. To fill this knowledge gap, this paper analyzes and illustrates in detail the seismic wave field at a construction site of the BARD Offshore 1 wind farm. For this purpose, the measured data from the construction site are compared to the results of a seismo-acoustic model. The measured and modeled data in combination provides a potential benchmark case for subsequent studies and other authors. The computed seismic wave field is investigated in terms of wave generation, mode composition, and propagation range of individual modes. The different seismic wave forms and their contribution to the particle motions in the seabed vicinity are discussed. The results indicate that, for the considered case, interface waves dominate the particle motion at the seafloor level up to a distance of 200 m.
 https://doi.org/10.1121/10.0025177
(Received 8 August 2023; revised 16 February 2024; accepted 19 February 2024; published online 7 March 2024)
[Editor: Stephen P. Robinson] Pages: 1856–1867

I. INTRODUCTION

The offshore wind energy is an important part of the future energy supply. For the foundation of offshore wind turbines in shallow waters which are typical for the North Sea and Baltic Sea piles are driven into the seabed. This process generates high levels of noise in the water column even at great distances to the pile, affecting marine mammals such as the harbour porpoise (Bailey *et al.*, 2010). In recent years, the particle motion associated with the pile driving and its effect on the marine fauna receive increasing attention. In particular, particle motion induced by seismic interface waves in the lower part of the water column and in the upper sediment layers (Hazelwood and Macey, 2016) has potential impacts on fish and aquatic invertebrates living near to or in the seabed, such as physical damage, physiological changes and behavioural changes (Hawkins *et al.*, 2021; Popper *et al.*, 2022; Roberts and Elliott, 2017; Roberts and Rice, 2023; Roberts and Wessel, 2023). In addition, it is not known whether seismic interface waves and the associated particle motion are reduced by noise abatement systems such as the bubble curtain (Bohne *et al.*, 2019, 2020; Peng *et al.*, 2021b).

The seismic interface waves that occur in the underwater environment are mainly Scholte and Stoneley waves. The two types of seismic waves are shown schematically in Fig. 1. They occur predominantly at low frequencies and induce elliptical particle motion. Scholte waves propagate at the water-sediment interface and create an evanescent sound field within the water column (Hazelwood and Macey, 2021). Stoneley waves propagate within the sediment at layer interfaces (Jensen *et al.*, 2011).

To the best of the authors' knowledge, detailed studies of the seismic wave field emitted during pile driving are mostly limited to the near-field of the pile. For example, Tsouvalas and Metrikine (2014) investigated the pile-water-sediment interaction using a semi-analytical vibroacoustic model. They observed various seismic waves, including Scholte waves and shear waves, in the sediment near the pile. In a subsequent publication (Tsouvalas and Metrikine, 2016), they made a first attempt to compare the results of the ground vibration modelling with measured data from an offshore wind farm in the North Sea. The modelling approach generally overestimated the ground vibrations, which they explained by the fact that no slip between the pile and the sediment has been considered. Addressing this issue, Molenkamp *et al.* (2023) introduced a contact relaxation condition in the form of a spring between the pile and the sediment surface. They found that by reducing the stiffness of the spring, the Scholte wave amplitude decreases, and the pile dynamics increase around the natural frequencies of the pile.

In general, the above studies of the seismic wave field are based on the assumption that the seabed can be described with sufficient accuracy as an elastic medium. This neglects some of the effects that occur in porous sandy

[a]Email: t.bohne@isd.uni-hannover.de

https://doi.org/10.1121/10.0025177

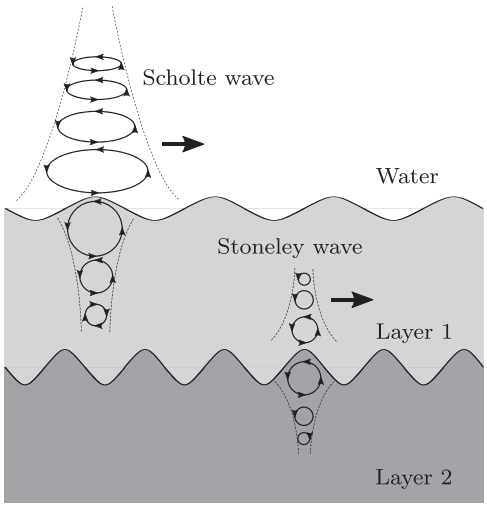

FIG. 1. Representative scheme of the Scholte wave and Stoneley wave, adapted from Meegan *et al.*, 1999 with the permission of the Acoustical Society of America. Copyright 1999, Acoustical Society of America.

sediments, which are very prevalent in coastal waters. In their recent publication, He *et al.* (2023) address this limitation by modelling the sediment as a poroelastic medium and comparing the results with those of an elastic sediment model. They found that the latter generally overestimates the sound pressure level for saturated sands, also for seismic interface waves.

In order to extend the consideration of seismic waves to distances beyond the immediate vicinity of the pile, Peng *et al.* (2021a) expanded the semi-analytical close-range model (CRM) proposed by Tsouvalas and Metrikine (2014) with a model based on wave number integration. Hence, the question arises up to what distance from the pile interface waves occur in real marine environments, and how far do they pose a potential threat to the marine fauna.

Measurements by Reimann and Grabe (2014) at the BARD Offshore 1 wind farm confirm that significant seafloor motions occur at small distances from the pile, which can be potentially attributed to seismic interface waves. Measurements by Bruns *et al.* (2014) show that significant low frequency ground vibrations due to interface waves can also occur at a distance of 750 m from the pile. Potty and Miller (2018) and Potty *et al.* (2023) detected interface waves at distances of 500 m and even at 1500 m from the pile, respectively.

Therefore, the aim of this work is to investigate in detail the generation and the propagation of the seismic interface wave field in the vicinity and at greater distances from the pile. This is done for a specific construction site at the BARD Offshore 1 wind farm in the North Sea for which extensive measurement data are available. For a single pile driving event, the pile dynamic, hydroacoustic, and ground vibration data are presented and compared with numerical results from a seismo-acoustic model. The combination of measured and modelled data establishes a potential benchmark case for subsequent studies and other authors. This is the first original contribution of this work. Based on the results, the contribution of the seismic interface waves to the particle motions in the seabed vicinity is discussed in detail. This is the second original contribution of this work.

This work is structured as follows. In the beginning, the seismo-acoustic model, hereafter referred to as the seismo-acoustic model for pile-driving (SAMPD), is presented in Sec. II. Then, the site conditions, the measurement concept, and the data processing are described in Sec. III. The measurement data are compared to the results provided by the SAMPD in Sec. IV. By means of the computed results, the seismic wave field is analysed in Sec. V. Finally, a conclusion is drawn in Sec. VI.

II. SAMPD

In order to simulate the wave field for a real offshore site with emphasis on the low-frequency seismic wave field and to compare the results with measurement results, in this work a SAMPD is developed. This includes a CRM accounting for the wave generation due to the interaction between the pile and the surrounding environment and a long-range model (LRM) representing seismo-acoustic wave propagation. The system is excited at the pile head with a forcing function derived from the impact hammer model of Fricke and Rolfes (2015).

The CRM has been set up in the finite element method solver COMSOL MULTIPHYSICS. The model domain has been defined in cylindrical coordinates r and z, assuming azimuthal symmetry. The origin is located at the crossing point of sea surface and symmetry axis whereby the positive z-coordinate points upwards. The domain comprises the pile, the water column, and the upper sediment layers. The pile axis coincides with the symmetry axis. The water is treated as a fluid medium. Hence, the Helmholtz equation is solved for the complex valued acoustic pressure $P(r,z,f)$. The pile and sediment are modelled as elastic media on basis of the equation of motion for an isotropic solid with the dependent field quantities radial displacement $U(r,z,f)$ and vertical displacement $W(r,z,f)$. The two physical systems are coupled by a fluid-structure-interaction condition.

Figure 2 shows the model domain with its dimensions and boundary conditions. At the pile head, the vertical forcing function F is defined. A pressure release condition is defined at the sea surface. To avoid reflections at the outer boundary of the domain, a perfectly matched layer (PML) is created at the right and lower edge of the domain. In front of the PML at the coupling radius r_c, the values of the field quantities are extracted from the CRM and passed to the LRM as starting field.

To account for contact relaxation between the pile and the sediment as suggested by Molenkamp *et al.* (2023), an elastic layer is introduced between the pile and the sediment. The elastic layer is set to act as a spring with the stiffness k_{EL} and as a viscous damping element with the damping constant d_{EL} on the vertical relative motion. Molenkamp *et al.* (2023) investigated the effect of various reductions in the static vertical stiffness of the sediment on pile vibrations

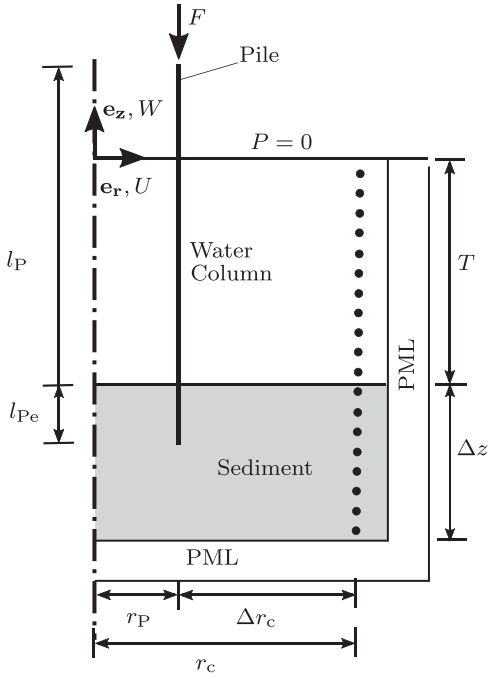

FIG. 2. Representative scheme of the parametrized source model domain with the applied boundary conditions. The dotted line denotes the coupling interface. The abbreviation PML stand for perfectly matched layer.

and seabed vibrations. However, they did not provide insights into a realistic value for the spring stiffness (k_{EL}). For simplicity, the static vertical stiffness of the sediment is reduced here to 50% of its original value using a spring stiffness with $k_{EL} = 1.13 \times 10^9\,\mathrm{N/m}$. To account for energy losses due to friction, a critical damping ratio is assumed ($d_{EL} = 4.78 \times 10^7\,\mathrm{Ns/m}$). For completeness, it is worth mentioning an approach which is an alternative to introducing spring and damping elements at the pile-sediment interface and has been used for a vibratory pile driving problem. In their recent work, Molenkamp *et al.* (2024) utilized the non-linear driveability model developed by Tsetas *et al.* (2023) to obtain a more realistic friction force. This was then used as an input to their noise prediction model. This approach has the advantage of avoiding the need to estimate or calibrate spring and damping coefficients, as is done in this case. Additionally, it allows for the consideration of more complex contact and friction effects, such as friction fatigue.

For the LRM, the higher-order elastic parabolic equation (HEPE) has been implemented. Since its introduction, this approach has been continuously developed until today (Collins, 1989, 1991, 1993a). It has been tested for various applications, which are characterised by shear waves and interface waves. Compared to other approaches, it is characterised by its versatility, as it can be used efficiently for laterally varying and thus real marine environments (Collins *et al.*, 2021).

The HEPE is derived in a similar way to the acoustic parabolic equation (Collins, 1993b). First, the elastic wave equation is factored to obtain the outgoing elastic wave equation. The resulting square root term is then approximated using the Padé series. The depth operator is discretised using the Galerkin method for variable grid size (Sanders and Collins, 2013). The HEPE is solved by forward integration using the Crank-Nicolson method. The Padé coefficients are obtained by the rotated rational approximation described in Collins (2015) and Collins *et al.* (2021). To ensure a good resolution of the shear wave field within the total field, the number of Padé coefficients in this work has been chosen to be $n_P = 20$.

Although the forward integration scheme guarantees an efficient solution, the computational times increase sharply with frequency for sediments with low shear wave velocities, such as sandy sediments ($c_s \ll c_c$). As a result, the HEPE is limited to the low frequency range. Since seismic interface waves dominate the wave field at greater distances from the pile only at low frequencies, this limitation is reasonable. Therefore, a critical frequency f_{crit} is introduced up to which the HEPE is solved. Beyond this critical frequency, the acoustic parabolic equation (PE) is used with split-step Padé integration (Collins, 1993b) and $n_P = 4$.

It should be noted that in this study the sediment is assumed to be an elastic isotropic medium. This allows the CRM and LRM to be based on the same physics, facilitating a direct and efficient coupling between the two domains. Additional poroelastic effects which are expected for saturated sandy soils, such as the one investigated in this work, are assumed to be rather small and maximal in the same order of magnitude. Considering Fig. 6 of He *et al.* (2023), quantitative deviations between the elastic and poroelastic sediment model can be observed. However, the signal characteristics remain similar. From the authors' perspective, it is therefore reasonable to assume that the sediment can be treated as isotropically elastic.

A. The coupling parameter Δr_c

The coupling distance Δr_c is an unknown modelling parameter that determines where the field values are extracted from the CRM and passed to the LRM as starting field. Following Fricke and Rolfes (2015), it should be chosen with respect to the far-field condition $k_0 r \gg 1$. In order to find a proper value for the coupling radius, a parameter study has been carried out with the SAMPD for exemplary center frequencies in the lower frequency range $f \in \{8, 16, 63\,\mathrm{Hz}\}$. In the study, the coupling radius is varied within the set $k_w \Delta r_c \in \{1, 2, \ldots, 10\}$. To account for the general frequency dependence of the results, a dimensionless form of the coupling distance is used. The model domain has been defined on the basis of the geoacoustic model shown in Fig. 7 and the pile dimensions have been chosen according to Table I.

To assess the accuracy of the SAMPD, the results from the parameter study are compared with a reference solution which has been obtained from the CRM, extended to $r = r_P + 60/k_w$. The corresponding model is hereafter referred

https://doi.org/10.1121/10.0025177

to as extended close-range model (eCRM). The normalized mean absolute error is used as measure for the accuracy,

$$nMAE = \frac{\sum_{i=1}^{m} |\hat{y}(x_i) - y(x_i)|\Delta x_i}{[\max(x_i) - \min(x_i)]} \cdot \frac{}{\max(y(x_i)) - \min(y(x_i))}. \quad (1)$$

With the index $i \in \{1, 2, 3, \ldots, m\}$, the reference solution $\hat{y}(x_i)$, the model solution $y(x_i)$, the grid point x_i, the grid point spacing Δx_i, and the number of grid points m.

The simulation data from the SAMPD and eCRM are analysed as follows. The variation of the absolute value of the radial displacement $U(r,z,f)$ and the vertical displacement $W(r,z,f)$ with depth is determined at four dimensionless distances from the pile, i.e., $k_w\Delta r \in \{12,\ 15, 20, 60\}$. For each depth-dependent profile obtained, the *nMAE* is calculated. In Fig. 3, the variation of the *nMAE* over the coupling radius $k_w\Delta r_c$ is shown exemplary for 16 Hz. Similar results have been obtained for the other frequencies also. The error decreases with increasing coupling distance for both field quantities. For $k_w\Delta r_c = 10$, the maximum error is less than 0.02. Therefore, in the following work, unless otherwise stated, the coupling distance is chosen as $\Delta r_c = 10/k_w$.

Figure 4 shows exemplary the depth dependent profiles for the coupling radius $k_w\Delta r_c = 10$, along with the corresponding eCRM results. For each radial distance from the pile, a good quantitative agreement between the SAMPD results and the reference solution can be observed.

B. The critical frequency f_{crit}

The procedure described in the Sec. II A, allows the influence of the shear and interface wave field to be investigated at greater distances from the pile, i.e., within the LRM. Figure 4 also shows displacement profiles where the sediment is modelled as a fluid and thus shear and interface waves are neglected. For the radial and, in particular, for the vertical displacement, a difference can be seen between the fluid sediment and the reference solution at the distances of

TABLE I. Model parameters of the pile and the MENCK MHU 1900S hammer. The blow energy, hammer mass, anvil mass and pile dimensions are from von Estorff *et al.* (2015). The hammer height is from Fricke and Rolfes (2015). The material parameters are from Zampolli *et al.* (2013).

Name	Parameter	Unit	BO1
Hammer			
Energy (Blow 1436)	E_{1436}	(kJ)	1380
Mass	m_H	(kg)	92 000
Height	h_H	(m)	10
Mass anvil	m_A	(kg)	45 000
Pile			
Length	l_P	(m)	85.10
Diameter	d_P	(m)	3.35
Embedded length	l_{Pe}	(m)	18.50
Wall thickness	t_{Pw}	(mm)	75
Density	ρ_P	(kg/m^3)	7700
Compression wave velocity	c_{cP}	(m/s)	5950
Shear wave velocity	c_{sP}	(m/s)	3240

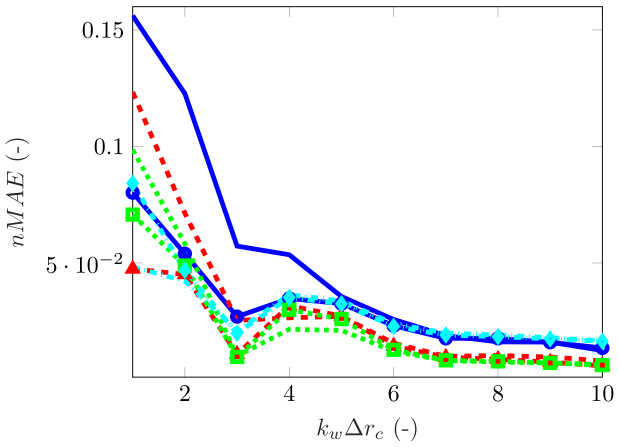

FIG. 3. (Color online) Variation of the normalized mean absolute error of the absolute value of the field quantities $U(r,z,f)$ and $W(r,z,f)$ over the dimensionless coupling radius $k_w\Delta r_c$ for 16 Hz at four dimensionless distances. $k_w\Delta r = 12$ ($U(r,z,f)$: -o-, $W(r,z,f)$: ——), $k_w\Delta r = 15$ ($U(r,z,f)$: -▲-, $W(r,z,f)$: – – –), $k_w\Delta r = 20$ ($U(r,z,f)$: ··□· $W(r,z,f)$: - - - - - -), $k_w\Delta r = 60$ ($U(r,z,f)$: -·◆·, $W(r,z,f)$: – – – -).

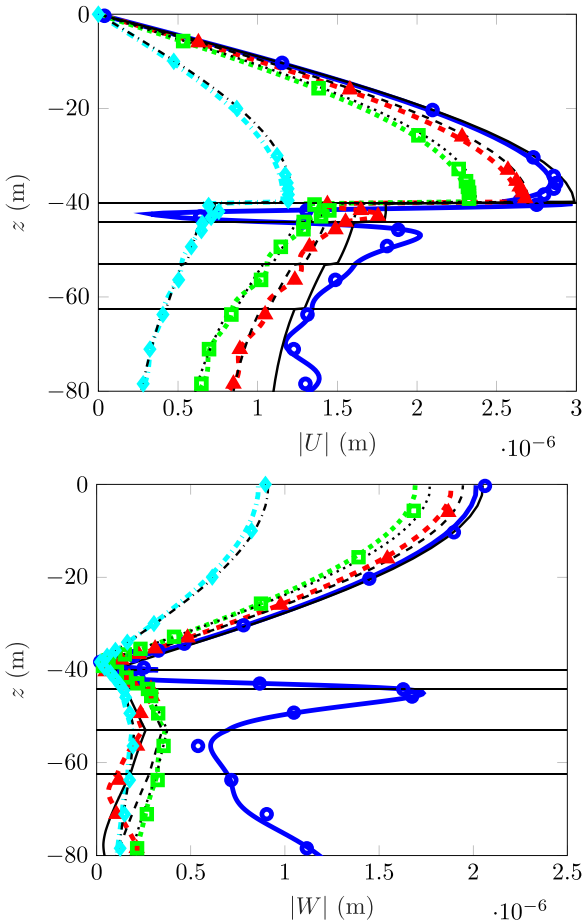

FIG. 4. (Color online) Variation of the absolute value of the vertical displacement $W(r,z,f)$ (bottom) and the radial displacement $U(r,z,f)$ (top) over the depth for the SAMPD, the extended eCRM and the SAMPD whereby shear effects are neglected in the LRM (PE). The coupling radius is $k_w\Delta r_c = 10$. The depth-dependent profiles are given for 16 Hz at four different dimensionless distances to the pile. $k_w\Delta r = 12$ (SAMPD: ——, eCRM: ○, PE: ——), $k_w\Delta r = 15$ (SAMPD: – – –, eCRM: △, PE: – – –), $k_w\Delta r = 20$ (SAMPD: - - - - - -, eCRM: □, PE: - - - - - - - -), $k_w\Delta r = 60$ (SAMPD: – – – -, eCRM: ◇, PE: – – – -).

$k_w\Delta r \in \{12, 15\}$. For larger distances, this difference almost disappears.

For further investigation, simulations have been performed for relevant mid-band frequencies, treating the sediment in the LRM as solid and fluid, respectively. The model domain has been defined on the basis of the geoacoustic model shown in Fig. 7 and the pile dimensions have been chosen according to Table I. Figure 5 shows the variation of the *nMAE* of the absolute value of the vertical displacement over the dimensionless distance from the pile. The solutions for the solid sediment are used as reference. A high error is observed at $k_w\Delta r = 11$. For frequencies $f \geq 16$ Hz, a continuous decrease in the error with distance from the pile can be observed. For $k_w\Delta r = 20$, the error is less than 0.015. The decrease can be explained by the high shear wave absorption reducing the shear and interface wavefield within the total field. Therefore, at greater distances from the pile the total field is dominated by the compressional wave field. In contrast, for lower frequencies ($f < 16$ Hz) a large error occurs even at greater distances from the pile. Thus, the critical frequency is chosen with $f_{\text{crit}} = 56$ Hz.

III. MEASUREMENTS AT A CONSTRUCTION SITE IN THE OFFSHORE WIND FARM BARD OFFSHORE 1 (OWF BO1)

Within the framework of the BORA project funded by the Federal Ministry for Economic Affairs and Climate Action, an extensive measurement campaign has been carried out at a construction site in the OWF BO1. Using a MENCK MHU 1900S hammer, a foundation pile with a length of approximately 85 m and an outer diameter of 3.35 m has been driven to the final embedded length of 34.6 m. During the ramming process, the pile dynamics, ground vibrations, and hydrosound emissions have been measured. Prior to construction, a geological survey has been carried out to determine the local sediment characteristics.

The hydroacoustic measurements have been conducted by the Institute for Technical and Applied Physics (ITAP). The measurements of the pile dynamics and ground vibrations in vicinity of the pile have been conducted by the Institute of Geotechnical Engineering and Construction Management of the Hamburg University of Technology. The geological survey has been carried out by the Workgroup Applied Geophysics of the Institute of Geosciences of the Kiel University.

Part of the data gathered in the project is evaluated in the following. A closer description of the project and measurement campaign can be found in the project report (von Estorff *et al.*, 2015) and measurement report (Bellmann *et al.*, 2013).

A. Measurement configuration and data processing

In this work, data sets from a few selected measurement stations are used. In Fig. 6, the names and positions of these measurement stations are given. The stations are identified by their original names from the project. Close below the pile head, the vertical pile acceleration has been measured by an accelerometer (E1B2). Within the water column the hydrosound pressure has been measured at three hydrophone measurement stations (MP1-MP3). At the seafloor, the vertical and radial velocity have been measured by two geophones (Lob2 and Lob3).

At each station, the signals were recorded for almost the entire pile-driving process. The first processing step has been to analyse the data and identify the signal segments for each hammer blow. For comparison with the SAMPD, the signal from the blow 1436 has been used as an example, corresponding to an embedded pile length of $l_{\text{Pe}} = 18.50$ m. At this point, the noise mitigation abatement system has been switched off.

The recorded signals from each measurement station have been processed as follows. The hydroacoustic signals have been high-pass filtered with a Butterworth filters of order 4 and a cut-off frequency of 5 Hz. The ground

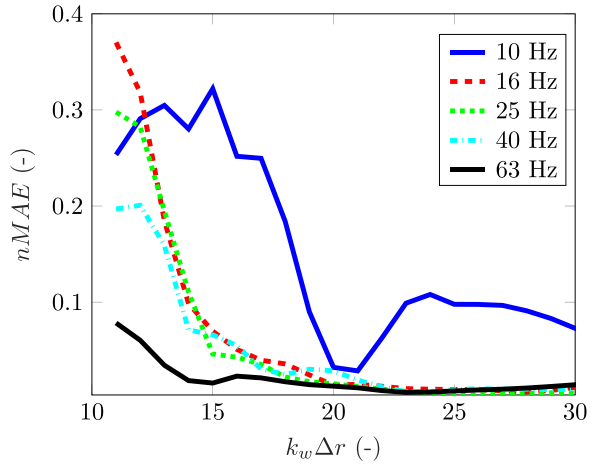

FIG. 5. (Color online) Variation of the normalized mean absolute error of the absolute value of the vertical displacement $W(r, z, t)$ over the dimensionless distance from the pile.

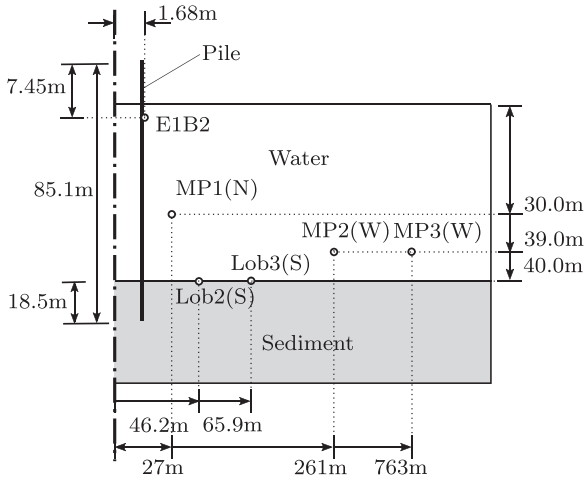

FIG. 6. Representative scheme of the pile and the measurement configuration at the considered construction site in the offshore wind farm BARD Offshore 1. The letters behind the names of the measurement stations indicate the cardinal direction.

https://doi.org/10.1121/10.0025177

vibration data have been high-pass and low-pass filtered with Butterworth filters of order 8 and cut-off frequencies of 5 and 56 Hz, respectively, taking into account the natural frequency ($f_n = 4.5$ Hz) of the sensor (von Estorff *et al.*, 2015). The upper frequency limit is the same as that used to investigate the ground vibration with the SAMPD. The pile acceleration signal from E1B2 shows a drift. To reduce the drift, the acceleration signal is first high-pass filtered with a Butterworth filter of order 4 and a cut-off frequency of 2 Hz. The filtered signal is then numerically integrated to give the uncorrected velocity signal. This is averaged using a moving window of 500 data points. The averaged signal is subtracted from the uncorrected velocity signal to give the final velocity signal.

B. Geoacoustic model

The OWF BO1 is located in the south-western region of the German Bight, with a water depth of around $T = 40$ m. The seabed in this area consists mainly of a thin top layer of silty sand and deeper sand layers. Podolski (2015) developed a geoacoustic model of the construction site based on the geological data. However, the geoacoustic model shows significant ranges of uncertainty in the shear wave velocity profile, particularly for the marine top layer and the adjacent sediment layer. For example, according to Podolski (2015), the shear wave velocity at the seafloor level is somewhere in the range of 25 to 165 m/s. Therefore, the shear wave velocity profile is re-determined here using the measured ground vibration and the SAMPD.

Taking into account the layer characteristics of the seafloor, the shear wave velocity profile is approximated by a simple two-layer profile consisting of a marine top layer and the underlying sediment. The shear wave velocities $c_{s,mtl}$ and c_s and quality factors $Q_{s,mtl}$ and Q_s are assumed to be constant within each layer. The subscript "mtl" denotes the marine top layer. In addition, the vertical dimension of the marine top layer Δz_{mtl} is considered. The five unknown sediment parameters are determined using a two-step parameter study.

In the first step, the shear wave velocities and the vertical dimension of the marine top layer, affecting mainly the interface wave propagation velocities, are varied within the sets $c_{s,mtl} \in \{30, 50, 70, 90\}$, $c_s \in \{150, 170, 190, 210, 230, 250\}$, and $\Delta z_{mtl} \in \{3, 4, 5\}$. The quality factors, which mainly influence the signal amplitudes, are left constant at the value 9, which has been found by Podolski (2015). For each of the resulting samples, a simulation has been carried out using the SAMPD. The calculated ground motions, i.e., the horizontal and vertical velocities, at the positions of Lob2 and Lob3 are compared with the corresponding measured data. Whereby, the data from blow 480, with an embedded pile length of $l_{Pe} = 10$ m, have been used. The level of agreement has been assessed quantitatively using the root mean square error (*RMSE*) of the normalised envelope of the velocity signals. In the second step, the quality factors $Q_{s,mtl}$ and Q_s have been varied each in the set $\{6, 8, 10, 12, 14, 18\}$. The level of agreement has been assessed quantitatively using the *RMSE* of the amplitude spectrum and the *RMSE* of the time signal of the velocities. Figure 7 shows the resulting geoacoustic model. The layering structure, compressional-wave properties and densities have been taken directly from Podolski (2015).

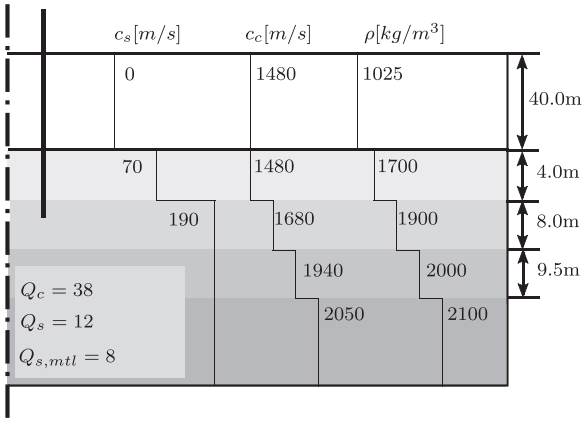

FIG. 7. Geoacoustic model of the construction site. The shear wave profile and the corresponding quality factors has been determined on basis of a parameter study. The compression wave velocity profile, the corresponding quality factor and the density profile have been taken from Podolski (2015).

IV. COMPARISON BETWEEN MEASURED DATA AND MODELLING RESULTS

In this section the SAMPD results are compared with the pile dynamic, hydroacoustic and ground vibration measurement data, cf. Sec. III. The model domain and the sediment material conditions have been set up on the basis of the geoacoustic model, cf. Fig. 7. The pile parameters have been chosen according to the project report of von Estorff *et al.* (2015), cf. Table I. The pile head forcing function for blow 1436 has been determined with the impact hammer model of Fricke and Rolfes (2015) on the basis of the parameters given in Table I. The resulting function is shown in Fig. 8. It should be noted that since the geoacoustic model has been partially fitted to the sediment vibration data, the modeled and measured data are not completely independent, cf. Sec. III B. Nevertheless, the comparison provides an opportunity to assess the plausibility of the modeling results.

Two model runs have been performed. Focusing on the seismic interface waves, which are dominant at low frequencies, a frequency range of 5.5 to 56 Hz has been investigated. The frequency spacing has been chosen to be $df = 0.25$ Hz. For the pile dynamics and the hydro sound emissions, a frequency range of 4 to 1100 Hz has been chosen. The frequency spacing has been increased to $df = 2$ Hz. The simulation results, shown below in the time domain, have been obtained by inverse Fourier transform. For the presentation of the acoustic data, the sound exposure level in one-third octave band L_{Ep} is used. The spectral density of the sound exposure level is written (Zampolli *et al.*, 2013)

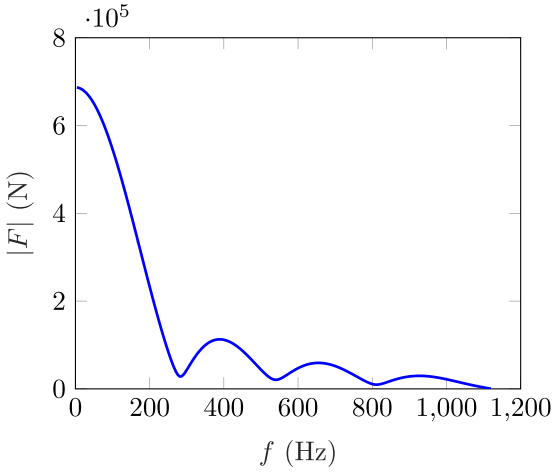

FIG. 8. (Color online) Variation of the absolute value of the pile head forcing function over frequency.

$$L_{\mathrm{E},p,\mathrm{d}} = 10\,\mathrm{lg}\,\frac{2\,|P(r,z,f)|^2}{\mu\,\mathrm{Pa^2s/Hz}} \tag{2}$$

with the sound pressure spectrum $P(r,z,f)$. The sound exposure level is obtained by integrating the term in the logarithm in Eq. (2) over the bandwidth.

Figure 9 shows the variation of the vertical pile velocity and acceleration at E1B2 over time. For the acceleration, the raw signal is given, cf. Sec. III A. The pile velocity is characterised by a prominent peak at around $t = 0.005$ s, which is caused by the downward travelling pulse, and a retarded oscillation at $t = 0.03$ s. Considering the pulse travelling time from E1B2 to the pile toe and back $2(85.1\,\mathrm{m} - 7.5\,\mathrm{m})/5950\,\mathrm{m/s} = 0.026$ s, the latter corresponds to the reflected pulse at the pile toe. Comparing the simulated data with measured data, a quantitative agreement for the peak and the pulse reflection can be observed for the velocity and the acceleration. However, a deviation can be observed in the range 0.01 to 0.02 s. Potentially, this can be explained by the varying wall thickness along the pile axis for the real pile which can cause partial reflections of the pulse wave. This has not been considered for the modeled pile.

Figure 10 shows the sound exposure levels in one-third octave bands at the measurement stations MP1–MP3. Two trends can be seen. First, the $L_{\mathrm{E},p}$ reaches its maximum at about 200 Hz for each measurement station. Second, the levels decrease with increasing distance. For MP1, there is a good quantitative agreement between the simulation and the measured data over the frequency range considered. For MP2 and MP3, the SAMPD underestimates the levels at higher frequencies ($f > 200$ Hz). This effect is more pronounced for MP3, which is located at a greater distance from the pile. This can be explained, by the compression wave velocity of the marine top layer. With a value of 1480 m/s, this is relatively low for sandy soils resulting in a higher sound transmission into the sediment.

In the next step, the ground motions at Lob2 and Lob3 have been examined. Figure 11 shows the variation of the vertical and radial velocity over time. In general, the signal

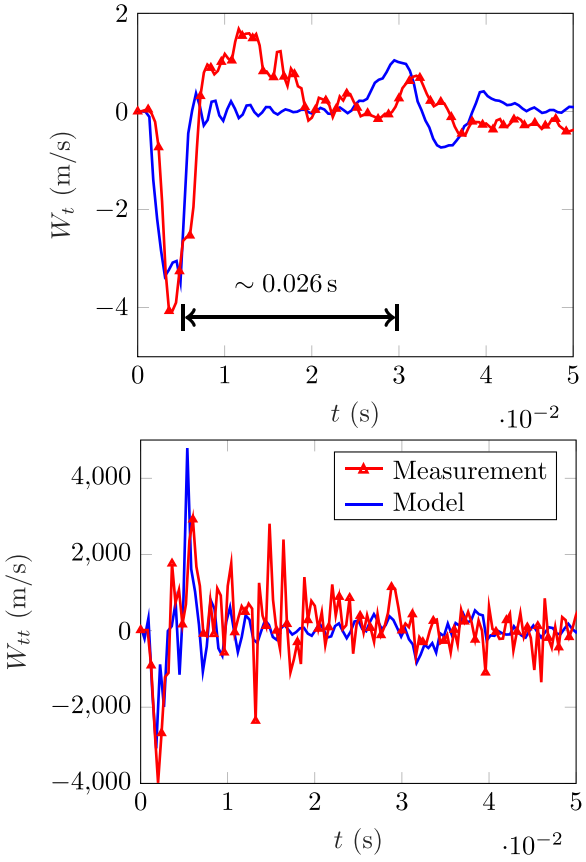

FIG. 9. (Color online) Variation of the vertical velocity (top) and vertical acceleration (bottom) over time at the measurement station E1B2 at the pile wall.

characteristics of the two velocities are similar. However, the radial velocities are much higher than the vertical velocities by a factor of 10. A splitting of the wave field can be observed. Within the time interval 0 s to 0.2 s a narrow peak can be observed, followed by high frequency oscillations which decay rapidly. This is followed by a low frequency oscillation which decays slowly. The first field can be associated with the primary compressional wave field and the

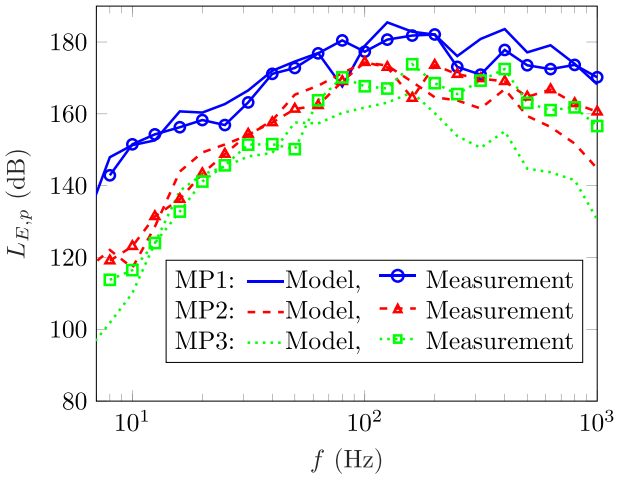

FIG. 10. (Color online) Sound exposure level in third octave bands.

https://doi.org/10.1121/10.0025177

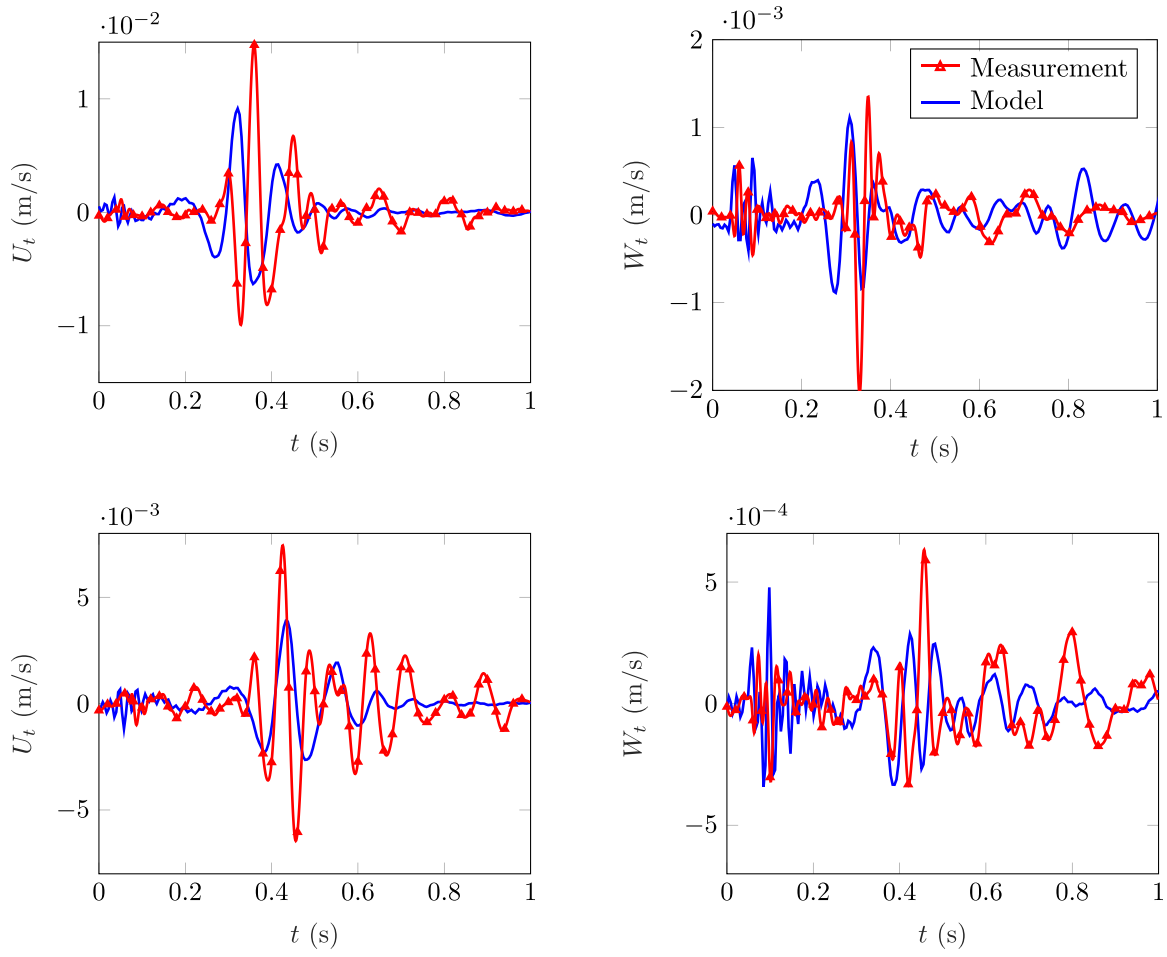

FIG. 11. (Color online) Variation of the radial velocity (left) and the vertical velocity (right) of the seafloor over time at the measurement stations Lob2 (top) and Lob3 (bottom), which are located at 46.2 m and 65.9 m distance from the pile, respectively.

second with shear and interface waves. A comparison of the simulated and measured data shows almost quantitative agreement. In particular, the envelope of the shear and interface wave field is accurately approximated. The maximum values of the radial displacement signals are fitted with less accuracy. Considering the complexity of the real seafloor, these deviations can be explained by the simplified modelling of the shear wave velocity profile as a two-layer profile.

Figure 12 shows exemplarily the amplitude spectra of the ground motions at Lob2. High amplitudes are observed for frequencies below 25 Hz. Considering the water depth, these correspond to the seismic wave field. Comparing the simulated and measured amplitudes, a higher agreement can be observed for lower frequencies. For the medium frequency range, the SAMPD underestimates the amplitudes. This can be explained possibly by the method used to determine the shear wave velocity profile. This is based on the envelope of the time signals which potentially is more sensitive to deviations at lower frequencies than at higher frequencies.

V. ANALYSIS OF THE SEISMIC WAVE FIELD

This section analyzes the computed seismic wavefield of Sec. IV, focusing first on the generation of the seismic wavefield at the pile-sediment interface and second on the mode composition of the wavefield over the range. Figure 13 shows the vertical particle velocity of the embedded pile and the motion of the adjacent sediment at two depths in the sediment. The pile and sediment motions are taken from two adjacent points. The first is in the center of the pile wall ($r = d_P/2 - t_{Pw}/2$) and the second is 10 cm from the outer diameter of the pile ($r = d_P/2 + 10\,\text{cm}$).

The motion of the pile is characterized by a prominent peak at about 0.018 s, caused by the downward travelling pulse wave, followed by a backswing due to the reflection of this wave at the pile toe. Due to the fact that the observation points are close to the pile toe, the two motions cannot be clearly separated. At 0.045 s, the wave reflected at the pile toe and then again at the pile head passes the points a third time. In general, the motion of the adjacent sediment follows the motion of the pile but is much smaller due to the contact relaxation included in the modeling approach, cf. Sec. II.

Considering the real nonlinear slip phenomenon of the pile, it would be expected that the velocity of the sediment and the pile are nearly the same, but separate at a certain point when yielding occurs in the sediment. The subsequent relative motion causes friction losses that dampen the pile

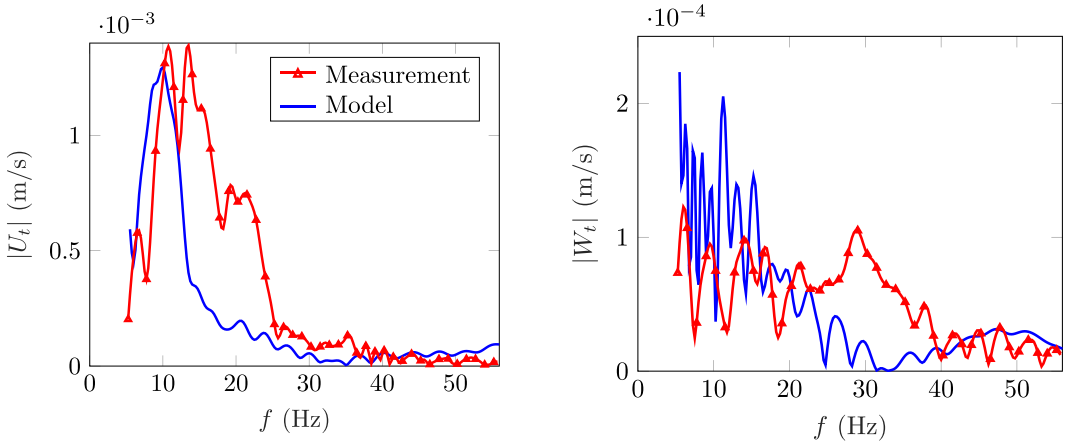

FIG. 12. (Color online) Variation of the absolute value of the Fourier transform of the radial velocity (left) and the vertical velocity (right) of the seafloor over frequency at the measurement station Lob2.

dynamics. Assuming that the energy transfer into the sediment is higher when the contact between the pile and the sediment is maintained, it could be possible that the smaller second and third passing waves radiate more energy into the sediment than the first wave causing the pile slipping. The latter is not accounted for by the contact relaxation used here. However, this linear approach, if well calibrated, could provide a method to properly account for at least part of the energy transfer process.

In the second step, the mode composition over the range within the seismic wave field is investigated. At first, the wave modes are identified and characterized. Figure 14 shows the time series of the radial and vertical velocity at the seafloor level ($z = -40$ m) for different ranges. For presentation purposes, all traces have been multiplied by the corresponding range value r according to Jensen *et al.* (2011). The signal splits into three wave packages as the range increases. The wave packages are numbered from one to three according to the time of their occurrence.

The first wave package propagates with a velocity of about 1500 m/s corresponding to the compressional mode. The second wave package propagates at 150 m/s. The third wave package propagates at about 50 m/s. Due to their low propagation speed the modes 2 and 3 correspond to shear or interface waves. For the two modes, a phase shift between the vertical and radial velocity of $\pi/2$ can be observed. This phase shift indicates an elliptical particle trajectory which is

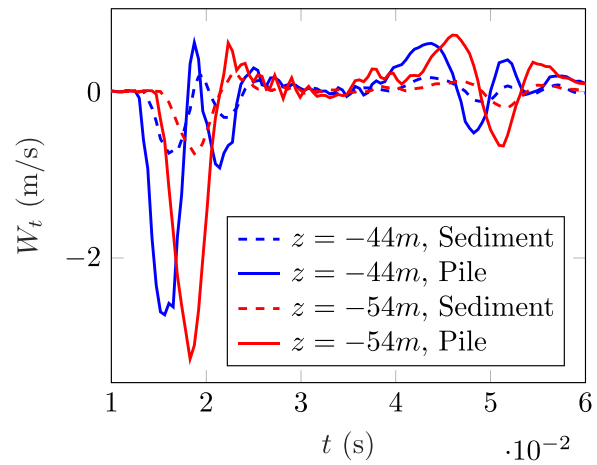

FIG. 13. (Color online) Variation of the vertical velocity of the pile and the adjacent sediment at two depths within the sediment.

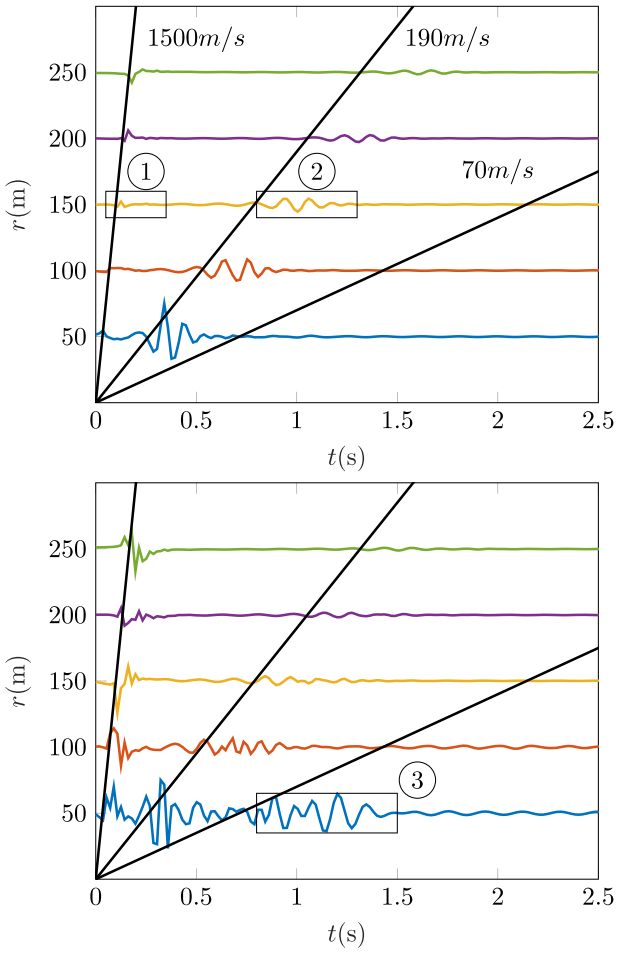

FIG. 14. (Color online) Stacked time series for the radial velocity (top) and vertical velocity (bottom) at the seafloor level ($z = -40$ m) and different ranges. The rectangles mark exemplary time sections of the mode signals. The circled numbers denote the mode numbers.

https://doi.org/10.1121/10.0025177

typical for interface waves (Achenbach, 1999; Meegan *et al.*, 1999). Figure 15 shows exemplary the normalized vertical and radial velocity profiles of the modes 2 and 3 over depth. For each mode, the profiles have been extracted from adjacent points in time, so that the time difference between both points roughly corresponds to the phase shift. Additionally, each point has been chosen in such a way that one of the velocities reaches a minimum or maximum value and the other velocity exhibits a value close to zero.

Observing the velocity profiles of mode 2 reveals a maximum vertical velocity at the interface between the marine top layer and the underlying sediment layer. This is followed, over time, by a minimum radial velocity within the marine top layer. This pattern corresponds to an elliptical counterclockwise motion of particles. Figure 16 illustrates the trajectories of representative particles. At the seafloor level ($z = -40$ m), one can observe nearly horizontal counterclockwise elliptical particle motion. As depth increases to $z = -45$ m, the particle motion transitions to a vertical motion, accompanied by a change from counterclockwise to clockwise motion. In particular, the particles in the water column remain almost stationary despite significant radial velocities at the sediment-water interface, which can be explained by the lack of shear strength of the water.

Similar observations concerning the particle motions can be made for mode 3, although this process is primarily associated with a region near the seafloor. Furthermore, the particles in the water column are influenced by the motion. Therefore, considering the propagation velocities and particle motion characteristics, mode 3 can be identified as a Scholte wave, while mode 2 can be identified as a Stoneley wave propagating at the interface between the marine top layer and the underlying sediment layer.

Regarding the variation of the mode composition of the wave field with distance to the pile, it can be seen in Fig. 14 that the Stoneley wave dominates the wave field at the seafloor level in addition to the compressional mode. The Stoneley mode can be detected in the signal up to a distance of 250 m from the pile. In contrast, the Scholte mode is no longer detectable in the signal at a distance of 100 m.

The question remains which mode most strongly influences the particle motion in the water column and the upper sediment layer. To characterise the particle motion, the mean square sound particle velocity level is chosen here which is defined as follows (ISO, 2017):

$$L_{E,u,i} = 10\,log_{10}\left(\int_{t_{i,min}}^{t_{i,max}} \delta_t(t)^2 dt/\delta_{t0}^2\right) \quad (3)$$

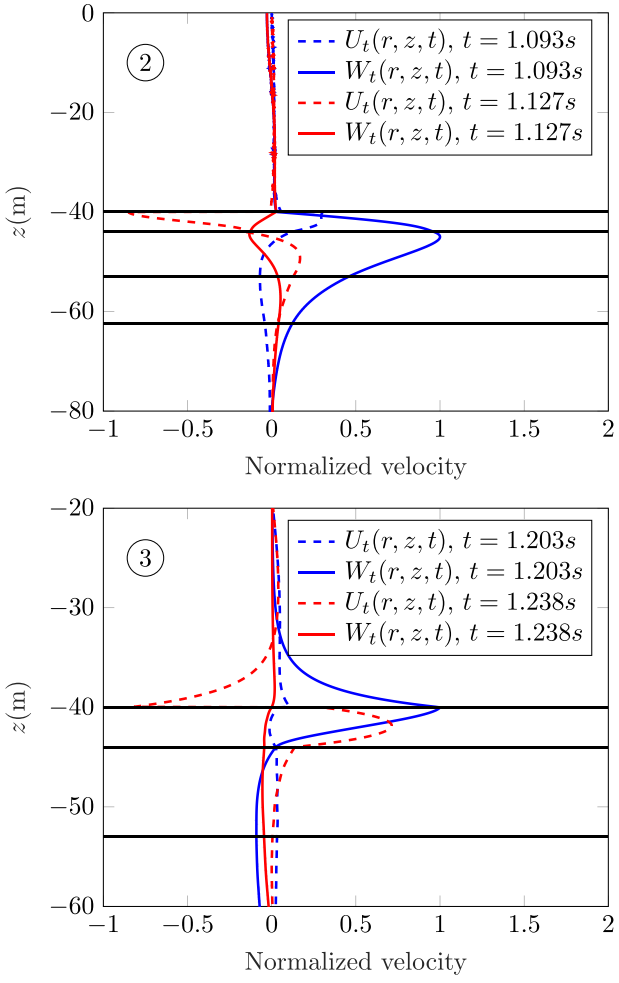

FIG. 15. (Color online) Normalized profiles of wave mode 2 (top) and 3 (bottom) over depth at the radial position $r = 150$ m and $r = 50$ m, respectively. The horizontal lines indicate the interfaces.

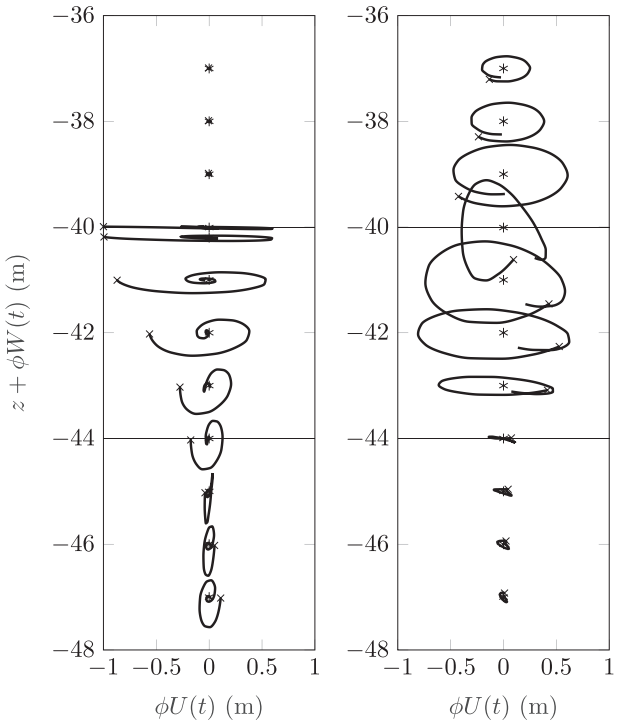

FIG. 16. Particle trajectories of mode 2 at $r = 150$ m (left) and mode 3 at $r = 50$ m (right) for the time intervals 1.033 to 1.257 s and 1.154 to 1.322 s, respectively. The asterisk denotes the equilibrium location. The symbol x denotes the starting point of the motion. The trajectories are scaled by the factor $\phi = 9.6291 \times 10^4$ and $\phi = 1.1497 \times 10^5$, respectively. The horizontal lines indicate the interfaces.

with the reference value $\delta_{t0}^2 = 10^{-9}\,\mathrm{m}^2/\mathrm{s}^2$ and the particle velocity

$$\delta_t(t) = \sqrt{U_t(t)^2 + W_t(t)^2}. \tag{4}$$

In the top part of Fig. 17, the variation of the mean square sound particle velocity level at the seafloor level over the radial distance from the pile is shown for the total time interval and for the time intervals of the modes. It can be seen that at the seafloor level the Stoneley mode dominates the particle motion up to a radial distance of 200 m. Beyond 200 m, the compressional mode dominates the sound particle velocity level. The point of intersection between the two modes has been used to specify the dominance. The Scholte wave has only a small effect on the total sound particle velocity level. This can be explained by the low shear wave velocity and the high shear absorption of the marine top layer. As a result, the Scholte wave is quickly absorbed and propagates only a short distance from the pile. It should be noted that these observations apply for the frequency range observed (5.5 to 56 Hz).

In the bottom part of Fig. 17, the sound particle velocity levels at a height of 1 m above the seafloor are shown. The compressional mode already dominates the particle motion beyond 50 m. Consequently, the Stoneley wave has minimal influence on the particle motion in the water column, as also observed in the particle trajectories.

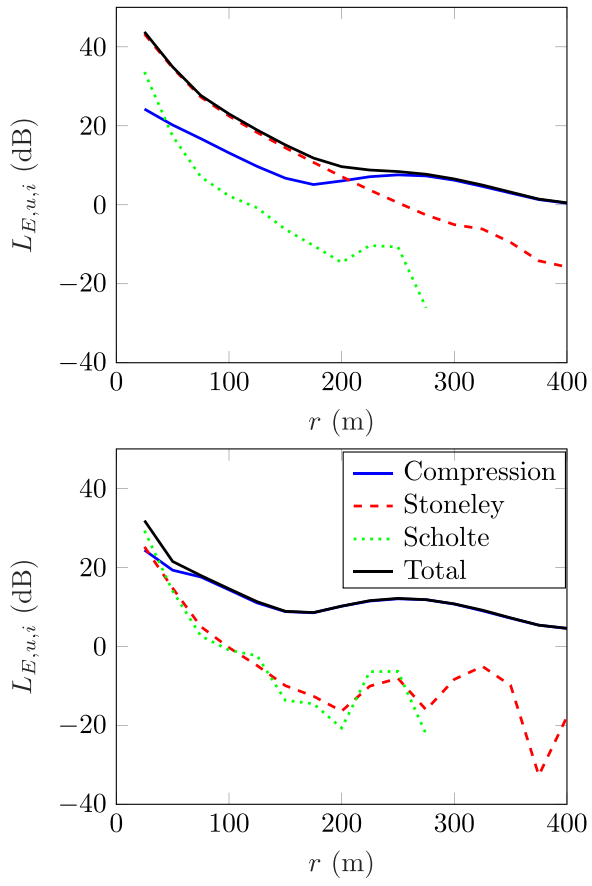

FIG. 17. (Color online) Variation of the mean square sound particle velocity level of the modes over the radial distance from the pile at the seafloor level (top) and at 1 m above the seafloor (bottom).

VI. CONCLUSION

The objective of this study was to conduct a detailed investigation of the low-frequency seismic wave field emitted by a pile during the driving process at a real construction site. For this purpose, a site laying within the BARD Offshore 1 wind farm was selected due to the availability of extensive pile dynamic, hydroacoustic, and ground vibration measurement data along with detailed information on the sediment.

To facilitate this investigation, a seismo-acoustic model was developed to simulate the interaction between the pile and its surrounding environment, as well as the propagation of seismic waves at greater distances from the pile. Emphasis was placed on a thorough comparison between the measured data and the computed results obtained from the seismo-acoustic model. Notably, the model accurately represents the signal characteristics, including the occurrence of high radial ground motions. The integration of both measured and modeled data establishes a potential benchmark case for subsequent studies and other authors.

A thorough investigation of the computed seismic wave field at the construction site was conducted, focusing on the wave generation and mode composition. In addition to the compressional mode, two other modes were observed and identified as the Scholte and Stoneley modes, respectively. The Stoneley mode was found to propagate at the interface between the marine top layer and the underlying sediment layer. To characterise these modes in terms of their propagation range and their influence on particle motion near or in the seafloor, the mean square sound particle velocity level was used. At the seafloor level, the Stoneley mode dominates the particle motion up to a distance of 200 m from the pile, resulting in significant radial particle velocities. Beyond 200 m, the compressional mode dominates the particle motion. Due to the lack of shear strength of the water, the particle motions in the water are almost unaffected by the Stoneley mode and are dominated by the compressional mode. In this study, the Scholte mode had a very small, negligible influence on the particle motions. This can be explained by the soft marine top layer of the considered site, which suppresses the propagation of the Scholte mode due to high shear absorption and low shear wave velocity.

ACKNOWLEDGMENTS

The Institute of Structural Analysis is part of the Center for Wind Energy Research For-Wind. Part of the research at Leibniz University Hannover was carried out in the frame of the BORA project in cooperation with project partners from the University of Kiel and the Hamburg University of Technology. Part of the measurement data used was acquired by the Hamburg University of Technology as part of the BORA research project. The authors gratefully

acknowledge the funding of the Federal Ministry for Economic Affairs and Climate Action due to an act of the German Parliament (project Ref. No. 0325421).

AUTHOR DECLARATIONS

Conflict of Interest

The authors state that they have no conflicts of interest.

DATA AVAILABILITY

The data that support the findings of this study are available within the article.

Achenbach, J. D. (**1999**). *Wave Propagation in Elastic Solids* (North-Holland, Amsterdam).
Bailey, H., Senior, B., Simmons, D., Rusin, J., Picken, G., and Thompson, P. M. (**2010**). "Assessing underwater noise levels during pile-driving at an offshore windfarm and its potential effects on marine mammals," Mar. Pollut. Bull. **60**(6), 888–897.
Bellmann, M. A., Guendert, S., and Remmers, P. (**2013**). "Offshore Messkampagne 1 (OMK 1) für das Projekt BORA im Windpark BARD Offshore 1" ("Offshore measurement campaign 1 (OMK 1) for the BORA project at the BARD Offshore 1 wind farm"), technical report.
Bohne, T., Grießmann, T., and Rolfes, R. (**2019**). "Modeling the noise mitigation of a bubble curtain," J. Acoust. Soc. Am. **146**(4), 2212–2223.
Bohne, T., Grießmann, T., and Rolfes, R. (**2020**). "Development of an efficient buoyant jet integral model of a bubble plume coupled with a population dynamics model for bubble breakup and coalescence to predict the transmission loss of a bubble curtain," Int. J. Multiphase Flow **132**, 103436.
Bruns, B., Stein, P., Kuhn, C., Sychla, H., and Gattermann, D. J. (**2014**). "Hydro sound measurements during the installation of large diameter offshore piles using combinations of independent noise mitigation systems," in *Proceedings of the 43rd International Congress on Noise Control Engineering* (November 16–19, 2014).
Collins, M. D. (**1989**). "A higher-order parabolic equation for wave propagation in an ocean overlying an elastic bottom," J. Acoust. Soc. Am. **86**(4), 1459–1464.
Collins, M. D. (**1991**). "Higher-order Padé approximations for accurate and stable elastic parabolic equations with application to interface wave propagation," J. Acoust. Soc. Am. **89**(3), 1050–1057.
Collins, M. D. (**1993a**). "An energy-conserving parabolic equation for elastic media," J. Acoust. Soc. Am. **94**(2), 975–982.
Collins, M. D. (**1993b**). "A split-step Padé solution for the parabolic equation method," J. Acoust. Soc. Am. **93**(4), 1736–1742.
Collins, M. D. (**2015**). "Treatment of ice cover and other thin elastic layers with the parabolic equation method," J. Acoust. Soc. Am. **137**(3), 1557–1563.
Collins, M. D., Lingevitch, J. F., and Calvo, D. C. (**2021**). "Fast and accurate seismic computations in laterally varying environments," IEEE Access **9**, 103258–103265.
Fricke, M. B., and Rolfes, R. (**2015**). "Towards a complete physically based forecast model for underwater noise related to impact pile driving," J. Acoust. Soc. Am. **137**(3), 1564–1575.
Hawkins, A. D., Hazelwood, R. A., Popper, A. N., and Macey, P. C. (**2021**). "Substrate vibrations and their potential effects upon fishes and invertebrates," J. Acoust. Soc. Am. **149**(4), 2782–2790.
Hazelwood, R., and Macey, P. (**2016**). "Modeling water motion near seismic waves propagating across a graded seabed, as generated by man-made impacts," J. Marine Sci. Eng. **4**(3), 47.
Hazelwood, R., and Macey, P. (**2021**). "Noise waveforms within seabed vibrations and their associated evanescent sound fields," J. Marine Sci. Eng. **9**(7), 733.
He, R., Xiang, Y., and Guo, Z. (**2023**). "A poroelastic model for near-field underwater noise caused by offshore monopile driving," J. Sound Vib. **564**, 117878.
ISO (**2017**). 18405:2017 "Underwater acoustics—Terminology (International Organization for Standardization, Geneva, Switzerland)."
Jensen, F. B., Kuperman, W. A., Porter, M. B., and Schmidt, H. (**2011**). *Computational Ocean Acoustics* (Springer, New York).
Meegan, G. D., Hamilton, M. F., Il'inskii, Y. A., and Zabolotskaya, E. A. (**1999**). "Nonlinear Stoneley and Scholte waves," J. Acoust. Soc. Am. **106**(4), 1712–1723.
Molenkamp, T., Tsetas, A., Tsouvalas, A., and Metrikine, A. (**2024**). "Underwater noise from vibratory pile driving with non-linear frictional pile–soil interaction," J. Sound Vib. **576**, 118298.
Molenkamp, T., Tsouvalas, A., and Metrikine, A. (**2023**). "The influence of contact relaxation on underwater noise emission and seabed vibrations due to offshore vibratory pile installation," Front. Mar. Sci. **10**, 1118286.
Peng, Y., Tsouvalas, A., Stampoultzoglou, T., and Metrikine, A. (**2021a**). "A fast computational model for near- and far-field noise prediction due to offshore pile driving," J. Acoust. Soc. Am. **149**(3), 1772–1790.
Peng, Y., Tsouvalas, A., Stampoultzoglou, T., and Metrikine, A. (**2021b**). "Study of the sound escape with the use of an air bubble curtain in offshore pile driving," J. Marine Sci. Eng. **9**(2), 232.
Podolski, C. (**2015**). "Beitrag geophysikalischer untersuchungen zur Rammschall-Prognose bei gründung von Offshore-Bauwerken" ("Contribution of geophysical investigations to pile-driving noise prediction for the foundation of offshore structures"), Ph.D. thesis, Christian-Albrechts-Universität zu Kiel, Kiel, Germany, https://macau.uni-kiel.de/receive/diss_mods_00018048?lang=de (Last viewed March 1, 2024).
Popper, A. N., Hice-Dunton, L., Jenkins, E., Higgs, D. M., Krebs, J., Mooney, A., Rice, A., Roberts, L., Thomsen, F., Vigness-Raposa, K., Zeddies, D., and Williams, K. A. (**2022**). "Offshore wind energy development: Research priorities for sound and vibration effects on fishes and aquatic invertebrates," J. Acoust. Soc. Am. **151**(1), 205–215.
Potty, G. R., and Miller, J. H. (**2018**). "Shear wave inversion using the horizontal to vertical ratio of Scholte wave particle velocity," in *OCEANS 2018 MTS/IEEE Charleston, IEEE*, Charleston, SC, pp. 1–4.
Potty, G. R., Miller, J. H., Lin, Y.-T., and Vigness-Raposa, K. (**2023**). "Interface wave contribution to acoustic particle motion during offshore wind farm construction," in *The Effects of Noise on Aquatic Life*, edited by A. N. Popper, J. Sisneros, A. D. Hawkins, and F. Thomsen (Springer International Publishing, Cham, Switzerland), pp. 1–9.
Reimann, K., and Grabe, J. (**2014**). "Sediment vibration due to offshore pile driving and induced underwater noise," in *Proceedings of the 2nd International Conference and Exhibition on Underwater Acoustics*, Rhodes, Greece, pp. 279–286.
Roberts, L., and Elliott, M. (**2017**). "Good or bad vibrations? Impacts of anthropogenic vibration on the marine epibenthos," Sci. Total Environ. **595**, 255–268.
Roberts, L., and Rice, A. N. (**2023**). "Vibrational and acoustic communication in fishes: The overlooked overlap between the underwater vibroscape and soundscape," J. Acoust. Soc. Am. **154**(4), 2708–2720.
Roberts, L., and Wessel, A. (**2023**). "Shaking up aquatic substrates: Taking lessons from biotremology and defining terminology," in *The Effects of Noise on Aquatic Life*, edited by A. N. Popper, J. Sisneros, A. D. Hawkins, and F. Thomsen (Springer International Publishing, Cham, Switzerland), pp. 1–15.
Sanders, W. M., and Collins, M. D. (**2013**). "Nonuniform depth grids in parabolic equation solutions," J. Acoust. Soc. Am. **133**(4), 1953–1958.
Tsetas, A., Tsouvalas, A., and Metrikine, A. V. (**2023**). "A non-linear three-dimensional pile–soil model for vibratory pile installation in layered media," Int. J. Solids Struct. **269**, 112202.
Tsouvalas, A., and Metrikine, A. (**2014**). "A three-dimensional vibroacoustic model for the prediction of underwater noise from offshore pile driving," J. Sound Vib. **333**(8), 2283–2311.
Tsouvalas, A., and Metrikine, A. (**2016**). "Structure-borne wave radiation by impact and vibratory piling in offshore installations: From sound prediction to auditory damage," J. Marine Sci. Eng. **4**(3), 44.
von Estorff, O., Grabe, J., Rolfes, R., Lippert, S., and Rabbel, W. (**2015**). "Final report of the joint research project BORA: Development of a computational model for the prediction of underwater noise due to pile driving for offshore wind turbine foundations," technical report.
Zampolli, M., Nijhof, M. J. J., de Jong, C. A. F., Ainslie, M. A., Jansen, E. H. W., and Quesson, B. A. J. (**2013**). "Validation of finite element computations for the quantitative prediction of underwater noise from impact pile driving," J. Acoust. Soc. Am. **133**(1), 72–81.